Green Chemistry Letters and Reviews

ISSN: (Print) (Online) Journal homepage: www.tandfonline.com/journals/tgcl20

Use of CeO_2 nanoparticles as CO_2-corrosion inhibitors of a duplex stainless steel

Alfredo Brito-Franco, Edna Vazquez-Velez, Roy Lopez-Sesenes, Ana Karen Larios-Gálvez, America Maria Ramirez-Arteaga & Jose Gonzalo Gonzalez-Rodriguez

To cite this article: Alfredo Brito-Franco, Edna Vazquez-Velez, Roy Lopez-Sesenes, Ana Karen Larios-Gálvez, America Maria Ramirez-Arteaga & Jose Gonzalo Gonzalez-Rodriguez (2024) Use of CeO_2 nanoparticles as CO_2-corrosion inhibitors of a duplex stainless steel, Green Chemistry Letters and Reviews, 17:1, 2360497, DOI: 10.1080/17518253.2024.2360497

To link to this article: https://doi.org/10.1080/17518253.2024.2360497

Published online: 31 May 2024.

GREEN CHEMISTRY LETTERS AND REVIEWS
2024, VOL. 17, NO. 1, 2360497
https://doi.org/10.1080/17518253.2024.2360497

Taylor & Francis
Taylor & Francis Group

Use of CeO_2 nanoparticles as CO_2-corrosion inhibitors of a duplex stainless steel

Alfredo Brito-Franco[a], Edna Vazquez-Velez[b], Roy Lopez-Sesenes[c], Ana Karen Larios-Gálvez[a], America Maria Ramirez-Arteaga[c] and Jose Gonzalo Gonzalez-Rodriguez[a]

[a]Universidad Autonoma del Estado de Morelos, CIICAp, Cuernavaca, Mexico; [b]Universidad Nacional Autónoma de Mexico, Instituto de Ciencias Fisicas, Cuernavaca, Mexico; [c]Universidad Autonoma del Estado de Morelos, FCQI, Cuernavaca, Mexico

ABSTRACT

The use of cerium oxide nanoparticles as a corrosion inhibitor for the CO_2 corrosion of LDX 2101 duplex stainless steel has been evaluated using potentiodynamic polarization curves, linear polarization resistance and electrochemical impedance spectroscopy tests. Polarization curves have shown that CeO_2 nanoparticles behaved as an efficient mixed type of inhibitor, with an efficiency that increases with its concentration reaching a maximum value when 600 ppm of nanoparticles were added. CeO_2 nanoparticles were chemically adsorbed onto the steel surface according to a Langmuir type of adsorption isotherm. A passive layer was formed by the addition of CeO_2 nanoparticles with lower passive current density and higher pitting potential values than those obtained without these nanoparticles. Corrosion current density decreased whereas the polarization resistance increased by two orders of magnitude in both cases with the addition of the nanoparticles. Similarly, the double layer capacitance was decreased due to the adsorption of the nanoparticles. Steel was susceptible to pitting type of corrosion, but its number and diameter decreased with the nanoparticles.

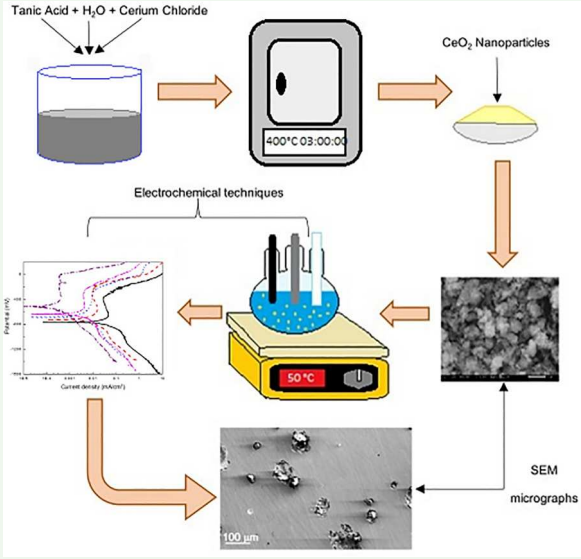

ARTICLE HISTORY
Received 12 February 2024
Accepted 22 May 2024

KEYWORDS
Duplex stainless steel; CO_2 corrosion; nanoparticles

1. Introduction

Corrosion of metals used in the oil and gas industries is a big problem, mainly due to the presence of gases such as CO_2 and H_2S, bringing both economic and environmental issues (1–5). Developing of dual stainless steels such as LDX 2101, were commercially introduced to improve both the mechanical properties and corrosion resistance of traditionally used austenitic stainless steels such as AISI 303 and 306 (6,7). Due to this, many research works are currently carried out to protect these metals against corrosion which includes the study of corrosion inhibitors. Among these compounds, there exist organic ones, such

CONTACT Jose Gonzalo Gonzalez-Rodriguez ggonzalez@uaem.mx Universidad Autonoma del Estado de Morelos, CIICAp, Av. Universidad 1001, 62209 Cuernavaca, Morelos, Mexico

as amines, amides, imidazolines, and ammonium quaternary salts (8–12), with the main drawback that they are toxic, expensive, and not environmentally friendly. To overcome this problem, some green inhibitors, such as plant extracts, coming from different parts of vegetables have been developed (13–22).

Among the different solutions to mitigate corrosion is the use of lanthanides, which have been to be efficient corrosion inhibitors for metals such as steel, galvanized steel, and aluminum among others (23–25). Among lanthanides, we can find Cerium (Ce) which can be found in two different oxidation states, Ce^{3+} and Ce^{4+}, which is an alternative to the use of Chromium not only because Cerium is not toxic but also because it can be found in commercial salts relatively cheap and readily available (26, 27).

Cerium dioxide (CeO_2) nanoparticles possess several eco-friendly aspects due to their unique properties and potential applications such as catalytic activity, which can be utilized in various eco-friendly processes. Some of these processes include catalytic converters in automobiles (28), Fuel Cell Applications (29), water treatment (30), or renewable energy technologies (31). Ce-based materials have different applications in preventing metal corrosion also such as coatings (32–39) and corrosion inhibitors (40–43) due to their chemical and physical properties which are related to the Ce electronic structure since it provides a barrier against corrosion in different aggressive environments (44–47). Thus, Fedel et al. (40) studied cerium oxide (CeO_2) nanoparticles (NPs) as corrosion inhibitors for mild steel in both sulfate and chloride-containing environments by using Open circuit potential (OCP) and Electrochemical impedance spectroscopy (EIS) studies. They found that the addition of NPs made the OCP value shift into the noble direction and an increase in the total impedance value, due to the formation of a passive layer on top of the steel. Sharmila et al. (41) use CeO_2 NPs as corrosion inhibitor for mild steel in Hydrochloric (HCl) and Sulfuric (H_2SO_4) acids by using the weight loss technique. They found that NPs exhibited a better performance in sulfuric than in hydrochloric acid, obtaining efficiency values of 99.73 and 83.55% respectively with the addition of 0.05 wt. % of CeO_2 NPs Bourenane et al. (42) evaluated the inhibitory action of cerium nanoparticles for steel in Ca $(OH)_2$ + 0.5 M $CaCl_2$ solution at 50°C by using potentiodynamic polarization curves and EIS tests. They found that the efficiency increased with the NPs concentration, reaching the highest efficiency with 800 ppm. Inhibitor acted as an anodic type of inhibitor which formed a layer of protective corrosion products by the physical adsorption of the nanoparticles. Thus, the goal of this work is to evaluate the corrosion efficiency of CeO_2 NPs as corrosion inhibitor for a LDX 2101 duplex stainless steel immersed in a CO_2-saturated 3.5 wt. % NaCl solution at 50°C with the use of electrochemical techniques.

2. Experimental procedure

2.1. Testing material

Working material included LDX2101 type duplex stainless steel containing (wt. %) 21.5 Cr, 5.0 Mn, 0.31 Mo, 1.5 Ni, 0.22 N, 0.026 C, 0.03 Si and Fe as balance. Specimens measuring 10.0 mm × 10.0 mm × 5.0 mm were spot welded to a copper wire, encapsulated in a commercial polymeric resin, grinded with 600 grade SiC emery paper, washed with water and acetone and blown with warm air.

2.2. Testing solution

As working electrolyte, a CO_2-saturated 3.5 (wt. %) NaCl solution at 50°C was used. Before testing, solution was bubbled with CO_2 during 2 h and kept bubbling during the whole testing time.

2.3. Cerium oxide nanoparticles synthesis

The precipitation method was used for the synthesis of the CeO_2 NPs, in which 0.5 g of Tannic acid was dissolved in 25 ml of deionized H_2O and kept under stirring. To this solution, 1.9 g of Cerium chloride ($CeCl_3$) was added, and, once dissolved, drops of 5% NaOH solution were added until the solution pH value was 8.0 ± 0.2. After this, the solution was centrifuged at 4000 rpm for 15 min to obtain a solid, which was washed with water and ethanol. This solid was dried at 80°C for 24 h in an electric furnace, and after that, it was calcined at 400°C during 3 h to obtain the CeO_2 NPs. Although some other Cerium oxides such as Ce_2O_3, CeO, Ce_3O_4, and CeO_3 can be obtained by the thermal decomposition of cerium salts, the most common are CeO_2 and Ce_2O_3, although the temperature required for the latter is 700°C. Other oxides such as CeO, Ce_3O_4, and CeO_3 are very unstable under normal conditions and it is not very common to find them. They were characterized by X-ray diffraction (XRD) and Transmission electronic microscopy (TEM) techniques. The X-ray patterns were obtained with an X-ray diffractometer Bruker d2phaser with a Cu Kα radiation source (λ = 1.54 Å) scanned during 10 min. NPs morphology and size analysis was performed in a Zeiss TEM using an acceleration voltage of 100 kV. For this, the CeO_2 NPs (2.5 mg) were dispersed in ethanol (5 ml), and 5 µL were taken and placed on a carbon-coated copper grid. A Raman confocal microscope Bruker Senterra II

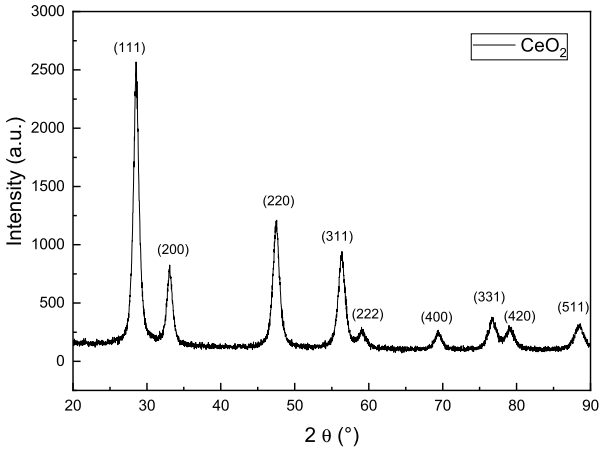

Figure 1. X-ray patterns of CeO_2 NPs.

was used for the chemical analysis of pure and corroded CeO_2 NPs. CeO_2 powder was focused with a 20 X objective, using a 785 nm laser with an aperture of 50 µm × 1000 µm, with a power of 100 mV, a resolution of 4 cm^{-1}, a spectral range from 400 to 3650 cm^{-1}, and an acquisition time of 3000 ms.

2.4. Electrochemical techniques

Electrochemical techniques used included potentiodynamic polarization curves, linear polarization resistance (LPR), and electrochemical impedance spectroscopy (EIS). For this purpose, a three-electrode standard glass cell was used, using a 6.00 mm graphite rod and a Silver/Silver chloride as counter and reference electrode respectively. Before starting the experiments, the open circuit potential value, OCP, was monitored during 3,600 s. Polarization curves were started by polarizing the specimen −1000 mV more negative than the free corrosion potential value, E_{corr}, scanned towards the anodic direction at a scan rate of 1 mV/s, and finishing at 1,000 mV more anodic than E_{corr}. Tafel extrapolation was used to calculate the corrosion current density values, I_{corr}. Inhibitor efficiency values, I.E., were calculated with the aid of following expression:

$$I.E.(\%) = \frac{I_{Corr1} - I_{Corr2}}{I_{Corr1}} \times 100 \quad (1)$$

where I_{corr1} and I_{corr2} are the corrosion current density values in the presence and absence of CeO_2 NPs respectively. For the LPR experiments, the specimen was polarized ± 15 mV around the E_{corr} value every 60 min during 24 h to obtain the polarization resistance value, R_p. Finally, the EIS measurements were carried out at the E_{corr} value by applying a perturbation signal of ± 15 mV in the frequency interval between 0.01 a 10,000 Hz. For the potentiodynamic polarization curves and LPR tests, a potentiostat from ACM instruments was used, whereas for the EIS experiments a potentiostat from Gamry instruments was used.

3. Results and discussion

3.1. Ceo_2 nanoparticles characterization

The X-ray pattern together with some micrographs of the CeO_2 NPs are given in Figures 1 and 2 respectively. X-ray pattern given in Figure 1 shows a characteristic peak for the CeO_2 NPs at a 2θ = 28.4° which corresponds to (111) plane. It is also shown the (200), (220), (311), (222), (400), (311), (420), and (511) planes, which represent the corresponding peaks for CeO_2 (48, 49). These peaks correspond to fluorite. No peaks corresponding to some other CeO_2 phases were detected, which means that synthesized CeO_2 NPs were pure and the detected peaks correspond to the crystalline fluorite phase only (50, 51). On the other side, Figure 2 shows SEM and TEM micrographs of CeO_2 NPs. SEM micrograph, Figure 2a, shows a uniform distribution of spherical structures composed of agglomerated particles, whereas TEM micrograph, Figure 2b, a spherical-

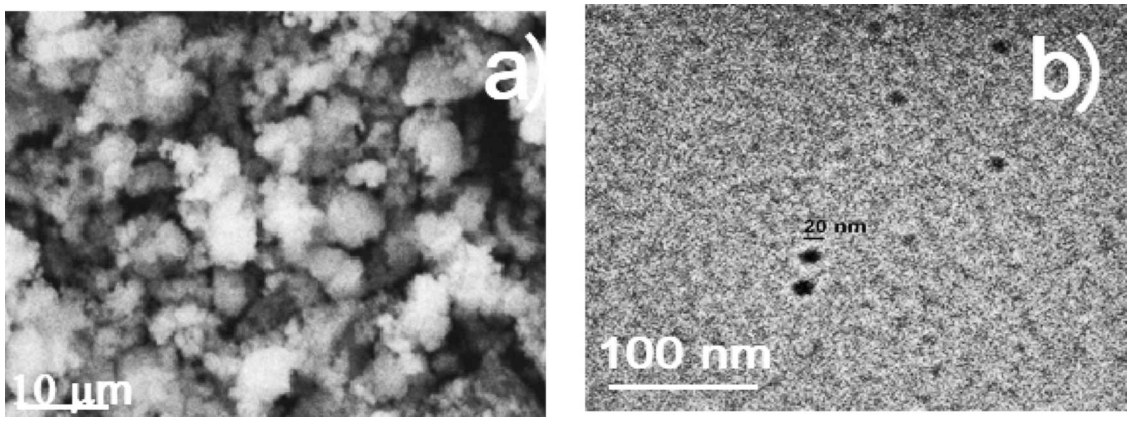

Figure 2. (a) SEM and (b)TEM micrographs of CeO_2 NPs.

shaped NPs with a size around 18–20 nm, with morphology as reported in the literature (52–54).

3.2. Open circuit potential

The effect of the CeO_2 NPs concentration on the open circuit potential value (OCP) for LDX 2101 type duplex stainless steel in a CO_2-saturated 3.5% NaCl solution is displayed in Figure 3. This figure shows that, for the blank, uninhibited solution, the OCP value starts in a very active value, around −750 mV, but rapidly it shifts into the noble direction, reaching a steady state value after approximately 2, 400 s. This shift into the noble direction indicates the formation of a very protective layer of corrosion products, which, in CO_2 environments, has been reported to be composed of some iron oxides such as FeO, Fe_3O_4, FeOOH, and $FeCO_3$ together with some chromium oxides/hydroxides, mainly CrO_3, Cr_2O_3, and $Cr(OH)_3$ (55). With the addition of either 200 or 400 ppm of CeO_2 NPs, the OCP value shifts in the noble direction, reaching higher values than that obtained in the absence of the nanoparticles, however, this value rapidly moves into the active direction, reaching values similar to those obtained in the uninhibited solution. The initial shift into nobler values indicates the formation of a more protective corrosion products layer than that formed in the uninhibited solution, whereas the shift of the OCP value into the active direction indicates the dissolution of this layer, indicating that this film of corrosion products is not protective enough. When either 600 or 800 ppm of CeO_2 NPs, the OCP value continuously moves into the noble direction, reaching steady state values very similar to each other, obtaining the noblest OCP value with these CeO_2 NPs concentrations, which is due to the formation of a very protective corrosion product layer. Thus, as we can see, generally speaking, the OCP value gets nobler as the CeO_2 NPs increase, just as reported by Fedel et al. (40).

3.3. Potentiodynamic polarization curves

The effect of CeO_2 NPs concentration on the polarization curves for LDX 2101 type duplex stainless steel in a CO_2-saturated 3.5% NaCl solution is shown in Figure 4 whereas electrochemical parameters are given in Table 1. It is clear from this figure, that, regardless of the presence or not of the CeO_2 NPs, curves display an active–passive behavior with the formation of a passive layer. As explained above, in the uninhibited solution, this passive layer consists of some iron oxides such as FeO, Fe_3O_4, FeOOH, and $FeCO_3$ together with some chromium oxides/hydroxides, mainly CrO_3, Cr_2O_3, and $Cr(OH)_3$ (55). From data given in Table 1, it can be seen that the E_{corr} value moves towards nobler values as the CeO_2 NPs increased, moving from a value of −770 mV obtained in the absence of nanoparticles to a value of −520 mV, obtained with the addition of 600 ppm of NPs; the E_{corr} value became more active with a further increase in the NPs concentration up to 800 ppm. The I_{corr} value decreased also with an increase in the CeO_2 nanoparticles, reaching its lowest value at 600 ppm of nanoparticles, with a value of almost one order of magnitude than that obtained in the uninhibited solution. An increase in the CeO_2 NPs concentration up to 800 ppm brought an increase in the I_{corr} value. The breakdown or pitting potential value, E_{pit} i.e. the potential value where the passive zone ends and an abrupt increase in the current density value is observed, increased,

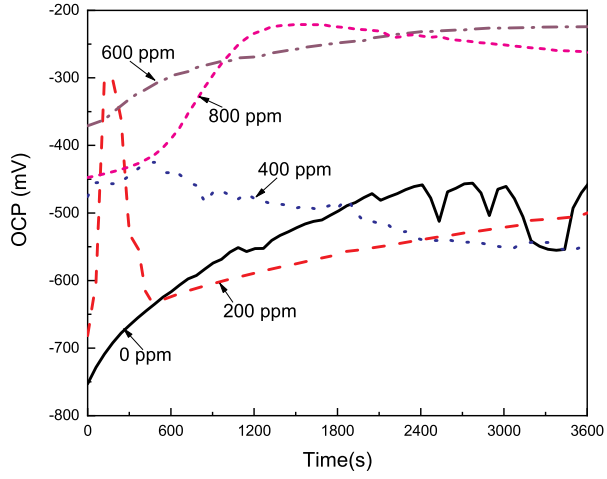

Figure 3. Effect of the CeO_2 NPs concentration on the OCP value for LDX 2101 duplex stainless steel in a CO_2-saturated 3.5% NaCl solution.

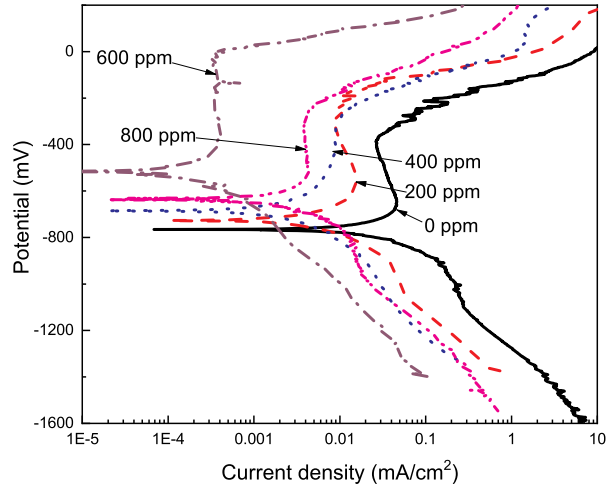

Figure 4. Effect of the CeO_2 NPs concentration on the polarization curves for LDX 2101 duplex stainless steel in a CO_2-saturated 3.5% NaCl solution.

Table 1. Electrochemical parameters obtained from polarization curves.

CeO_2 conc. (ppm)	E_{corr} (mV)	I_{corr} (mA/cm^2)	E_{pit} (mV)	β_a (mV/dec)	β_c (mV/dec)	I.E. (%)	θ
0	−770	3×10^{-2}	−375	125	−330	–	–
200	−730	8×10^{-3}	−280	115	−310	73	0.73
400	−680	5×10^{-3}	−270	100	−305	83	0.83
600	−520	2×10^{-4}	0	80	−290	99	0.99
800	−630	3×10^{-3}	−260	90	−280	93	0.93

becoming nobler as the CeO_2 NPs concentration increased, reaching its highest value at a concentration of 600 ppm, and it decreased with a further increase in the CeO_2 concentration of 800 ppm. Both, anodic and cathodic Tafel slopes were affected, therefore we can say that CeO_2 NPs behave as a mixed type of corrosion inhibitor affecting both, anodic steel dissolution and cathodic electrochemical reactions, which includes the dissociation of carbonic acid (H_2CO_3) into carbonate, bicarbonate ions, and protons to allow the hydrogen evolution reaction. Anodic dissolution or oxidation of iron is:

$$Fe \rightarrow Fe^{2+} + 2e^- \quad (2)$$

whereas cathodic reaction starts with the dissolution of CO_2 into the liquid phase is the initial step of CO_2 corrosion followed by the formation of carbonic acid (H_2CO_3) by the CO_2 hydration as follows (40):

$$CO_2 + H_2O \rightarrow H_2CO_3 \quad (3)$$

After this, carbonic acid dissociates to give bicarbonate ion, HCO_3^-, carbonate ion, CO_3^{2-} and protons, H^+ (43–45).

$$H_2CO_3 \rightarrow H^+ + HCO_3^- \quad (4)$$

$$HCO_3^- \rightarrow H^+ + CO_3^{2-} \quad (5)$$

$$H^+ + e^- \rightarrow 1/2 H_2 \quad (6)$$

The diffusion of H^+ ions from the bulk solution to the metal surface is responsible for the observed cathodic limit current whereas the contribution of the carbonic acid dissociation is minimal. The formation of carbonate scales on the metal surface can provide some protection against further corrosion, although it may also lead to localized corrosion underneath the scale if defects are present. The entry of hydrogen atoms into the steel is also possible, inducing some hydrogen embrittlement problems. On the other hand, in an H_2S-containing environment, the presence of H_2S enhances the anodic dissolution of iron, where sulfur induces the breakdown of the passive film, with the formation of corrosion products such as iron sulfide, FeS; however, there are many different kinds of iron sulfide compounds with different corrosion properties, and it has been suggested that, depending upon the environmental features, these corrosion products can have a similar effect to that of the passive films formed on top of stainless steels, decreasing the corrosion rate (27, 28). Due to the presence of other alloying elements such as Cr, Mn, and Ni, it is expected to have some nickel, manganese and chromium sulfides in addition to iron sulfide. However, chromium sulfides are thermodynamically unstable (32), and instead of chromium sulfides, a layer of chromic oxide is expected, which might be responsible for the passive behavior (33, 34).

Inhibitor efficiency value increased with an increase in the CeO_2 NPs, reaching a maximum value of 99% at a concentration of 600 ppm, decreasing down to 93% with a further increase in the NPs concentration of 800 ppm. Finally, the metal surface area covered by the inhibitor, θ, which is obtained by dividing the inhibitor efficiency value by 100, also increased with the NPs concentration, obtaining its highest value at a concentration of 600 ppm, decreasing once again at a concentration of 800 ppm.

3.4. Adsorption isotherm

Since we are assuming that the reduction in the I_{corr} value in the present research work is due to the adsorption of the CeO_2 NPs, we tried to adjust the data to different adsorption isotherms, including Langmuir, Tempkin, and Frumkin, and, as it can be seen in Figure 5, the best fitting was obtained with the Langmuir type of adsorption isotherm. The Langmuir isotherm is

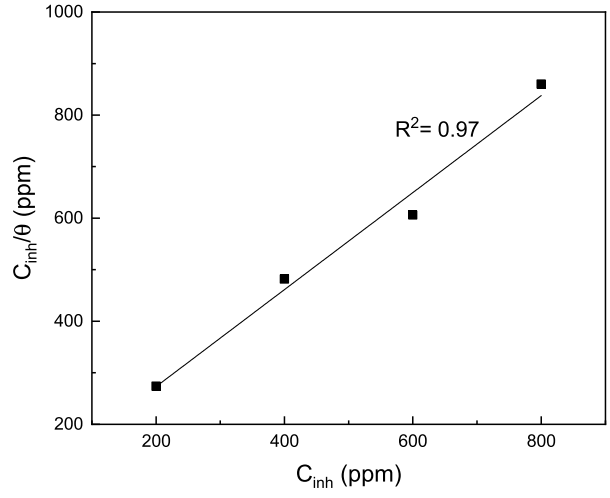

Figure 5. Langmuir adsorption isotherm for LDX 2101 duplex stainless steel in a CO_2-saturated 3.5% NaCl solution containing CeO_2 NPs.

represented, mathematically, as follows (56):

$$\frac{C_{inh}}{\theta} = \frac{1}{K_{ads}} + C_{inh} \quad (7)$$

where C_{inh} represents the inhibitor, CeO_2 nanoparticles concentration, θ stands for the fraction of metal surface covered by the inhibitor, and K_{ads} denotes the adsorption constant. The standard free energy ΔG^0_{ads} can be determined using the formula:

$$\Delta G^{\circ}_{ads} = -RTln(10^6 K_{ads}) \quad (8)$$

A plot of $C_{inh}/\theta - C_{inh}$, with the intersections of straight lines on the axes, enables the extraction of K_{ads} values and the water concentration in the solution (106 mg/L) using the universal gas constant (R) and the absolute temperature (T). Calculated ΔG^0_{ads} value was −40.31kJ mol^{-1}. For values of ΔG^0_{ads} around – 20 kJ mol^{-1} or less negative, the adsorption is considered to be physisorption, while values around −40 kJ mol^{-1} or more negative indicate chemisorption (56). This phenomenon confirms that the adsorption is a chemical type. The negative value of the ΔG^0_{ads} value indicates that the adsorption of CeO_2 NPs on the LDX 2101 type duplex stainless steel surface is spontaneous one.

3.5. LPR experiments

Potentiodynamic polarization curves are a kind of instantaneous picture of the corrosion phenomenon occurring on the steel surface. To know the change in the corrosion rate with time, some LPR experiments were carried out to know the polarization resistance value, R_p, we can have an idea of the change in the dissolution rate of the steel with time since R_p is inversely proportional to I_{corr}. The change in the R_p value with time for LDX 2101 type duplex stainless steel in a CO_2-saturated 3.5% NaCl solution at different CeO_2 NPs concentrations is shown in Figure 6. This figure shows that the R_p value increases as the CeO_2 NPs increases reaching its maximum value, for two orders of magnitude, at a concentration of 600 ppm, decreasing with a further increase in the NPs concentration. These results are in agreement with the I_{corr} values obtained from the polarization curves. For the uninhibited solution, the R_p value increases in a monotonically way due to the formation of protective corrosion products such as FeO, Fe_3O_4, FeOOH, $FeCO_3$, CrO_3, Cr_2O_3, and $Cr(OH)_3$. With the addition of CeO_2 NPs in concentrations different to 600 ppm, the R_p value increases also due to the adsorption of these NPs, but, after a while, around 10 h, this value decreases, probably due to the desorption of the CeO_2 NPs. However, for a CeO_2 NPs concentration of 600 ppm, the R_p value increases continuously as time elapses and remains stable due to the adsorption of these nanoparticles to form a layer that protects the steel from the aggressiveness of the environment.

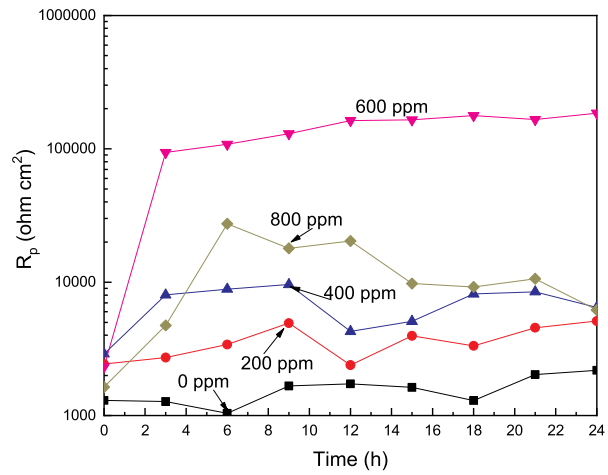

Figure 6. Effect of the CeO_2 NPs concentration on the R_p value for LDX 2101 duplex stainless steel in a CO_2-saturated 3.5% NaCl solution.

3.6. EIS tests

To have an insight into the corrosion mechanism occurring during the addition of the CeO_2 NPs during the corrosion of LDX 2101 type duplex stainless steel in a CO_2-saturated 3.5% NaCl solution, it was necessary to carry out some Electrochemical impedance spectroscopy tests. The results, in the absence and presence of the CeO_2 NPs are displayed in Figures 7 and 8 respectively in both Nyquist and Bode formats. For uninhibited solution, Figure 7a, Nyquist diagrams show the presence of a single, depressed, capacitive-like semicircle at all frequency values, indicating that the corrosion process is under charge transfer control. The semicircle shape did not change as time elapsed, indicating that the corrosion mechanism remained unaltered. Semicircle diameter increased as time elapsed due to the formation of a protective corrosion products layer as described above, and the increment in the semicircle diameter is due to the increment in the thickness of this layer. On the other hand, Bode plots in the impedance/modulus format, Figure 7b, show an increment on the total impedance value as time elapsed reaching its maximum value after 24 h of testing. This plot shows the presence of two different slopes, indicating the presence of two different time constants, Phase angle plots, on the other hand, show that this value remains very constant on a very wide interval of frequency values, indicating two-time constants, due to the presence of a very protective corrosion products layer typical of duplex stainless steels,

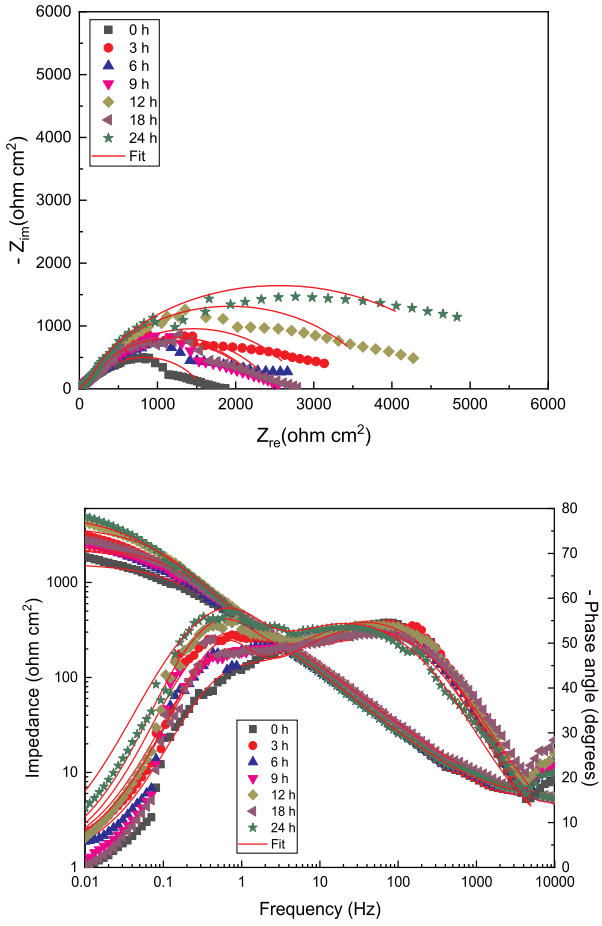

Figure 7. (a) Nyquist and (b) Bode diagrams for LDX 2101 duplex stainless steel in uninhibited CO_2–saturated 3.5% NaCl solution.

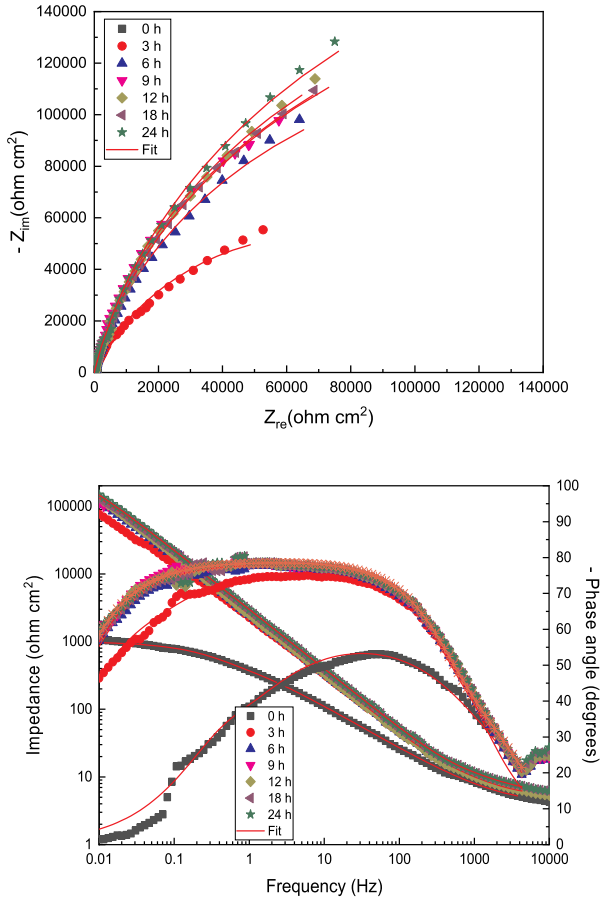

Figure 8. (a) Nyquist and (b) Bode diagrams for LDX 2101 duplex stainless steel in CO_2-saturated 3.5% NaCl solution containing 600 ppm of CeO_2 NPs.

and that this value increases as time elapses, reaching its highest value of 60° after 24 h of testing.

Since the lowest I_{corr} and highest R_p values were obtained with the addition of 600 ppm of CeO_2 NPs, corresponding EIS data at this concentration was chosen and they are displayed in Figure 8. As it can be seen, Nyquist plots, similar to the data found in absence of inhibitor, displayed a single depressed, capacitive semicircle at all the frequency values, indicating that the corrosion mechanism was the same as in the uninhibited solution, a charge transfer controlled one. The shape of these semicircles did not change with time, so the corrosion mechanism remained unaltered. The semicircle diameter increased as time elapsed due to the adsorption of the inhibitor and the formation of a very protective corrosion products layer. Due to this, the total impedance value increased as time elapsed, obtaining values almost two orders of magnitude higher than those found in the uninhibited solution as shown by the Bode plots, Figure 8a. Similar to the data given in absence of inhibitor, angle phase values increased with time and remained quite constant over a very wide interval of frequencies, obtaining values close to 80°, higher than those exhibited in the uninhibited solution, due to the adsorption of the CeO_2 nanoparticles and the formation of a much more protective corrosion products layer. It is clear the presence of two overlapped peaks in this plot, and, thus, the presence of two time constants.

Electrified interfaces such as those occurring during metal corrosion can be simulated by a combination of resistances and capacitors as shown in the electric circuit given in Figure 9. In this figure, the solution, corrosion products film, and charge transfer resistances are represented by R_s, R_f, and R_{ct} respectively, whereas the corrosion products film and double layer capacitances

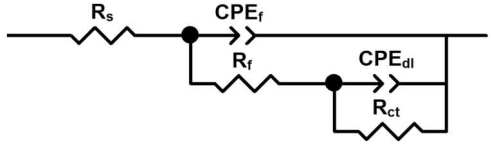

Figure 9. Electric circuit to simulate the EIS data.

Table 2. Electrochemical parameters obtained from fitting the EIS data for uninhibited solution.

Time (h)	R_s (ohm cm^2)	CPE_{dl} (F/cm^2)	n_{dl}	R_{ct} (ohm cm^2)	CPE_f (F/cm^2)	n_f	R_f (ohm cm^2)
0	4.9	4.88×10^{-4}	0.7	341	4.69×10^{-4}	0.8	1015
3	4.8	4.60×10^{-4}	0.7	455	3.19×10^{-4}	0.8	1605
6	4.8	4.20×10^{-4}	0.7	614	2.98×10^{-4}	0.9	1630
9	4.8	4.03×10^{-4}	0.7	687	2.87×10^{-4}	0.9	1738
12	5.0	3.66×10^{-4}	0.7	724	2.00×10^{-4}	0.9	2516
18	4.9	3.44×10^{-4}	0.7	755	2.22×10^{-4}	0.9	3272
24	5.2	2.88×10^{-4}	0.7	836	1.20×10^{-4}	0.9	4363

are represented by C_f and C_{dl} respectively. However, metal surfaces are not homogenous, instead, they have some heterogeneities such as roughness due to the electrolyte aggressiveness and ideal capacitances are replaced by constant phase elements, CPE, such as CPE_f and CPE_{dl}. The impedance of a constant phase element, Z_{CPE}, is calculated by using (57):

$$Z_{CPE} = \frac{(j\omega)^n}{Y_0} \tag{9}$$

where Y_0 is a proportionality constant, ω the angular frequency, $j = -1^{1/2}$and n the shift factor. Parameters obtained from fitting the EIS data by using electric circuit displayed in Figure 9 are summarized in Tables 2 and 3 for the tests in the absence and presence of 600 ppm of CeO_2 NPs respectively. In both cases, in the uninhibited and inhibited solution, the values for R_f are much higher than those for R_{ct}, indicating that the corrosion resistance is given by the corrosion products film. Additionally, both resistance values increased as time elapsed in both solutions. The increase in the R_f value for the uninhibited solution was only 4 times, whereas in the inhibited solution was more than two orders of magnitude, which is due to the adsorption of the CeO_2 nanoparticles and the formation of a very protective layer of corrosion products with a thickness that increases as time elapsed. On the other hand, the increase in the R_{ct} value is due to the formation of a barrier against the charge and mass transfer in the metal–electrolyte interface, protecting the metal from corrosion. Conversely to the resistance values, the CPE_f and CPE_{dl} values decreased as time elapsed in both uninhibited and inhibited solutions, and they were much smaller in the inhibited solution. The decrease in the CPE_{dl} values in the inhibited solutions is due to the adsorption of the CeO_2 NPs on the steel surface, displacing water molecules, and, since the size of the NPs is bigger than that for the water molecules, this brings to an increase in the double electrochemical layer thickness, which leads to a decrease in the double layer capacitance according to the following expression (58):

$$C_{dl} = \left(\frac{\varepsilon\varepsilon_0}{\lambda}\right)A \tag{10}$$

where ε_0 is the free space permittivity, ε the dielectric constant of that space, l the thickness of the double layer and A the electrode surface area. On the other hand, n_{dl} values close to 0.5 imply a high surface roughness due to a metal high dissolution rate, whereas a value close to 1.0 indicates a low surface roughness due to a low steel dissolution rate. From Tables 2 and 3 it can be seen that in the absence of CeO_2 NPs, the n_{dl} value is 0.7, close to 0.5, indicating a high steel surface roughness due to a high steel corrosion rate, whereas in the presence of 600 ppm of CeO_2 NPs, after 3 h of testing, the ndl value is 0.9, implying a low steel surface roughness due to a low corrosion rate.

3.7. Surface morphology studies

SEM micrographs of corroded specimens in the absence and presence of CeO_2 NPs are shown in Figure 10. It can be seen that, in all cases, except for corroded specimen in the presence of 600 ppm of nanoparticles, the steel exhibited pits on its surface. Thus, in the uninhibited solution, Figure 10a, the steel surface showed the highest

Table 3. Electrochemical parameters obtained from fitting the EIS data for tests containing 600 ppm of CeO_2 NPs.

Time (h)	R_s (ohm cm^2)	CPE_{dl} (F/cm^2)	n_{dl}	R_{ct} (ohm cm^2)	CPE_f (F/cm^2)	n_f	R_f (ohm cm^2)
0	3.6	3.02×10^{-4}	0.7	6	3.41×10^{-4}	0.7	1117
3	5.7	8.84×10^{-5}	0.9	8	8.78×10^{-5}	0.8	95,020
6	5.5	4.83×10^{-5}	0.9	16	3.05×10^{-5}	0.9	180,240
9	5.5	4.59×10^{-5}	0.9	17	2.94×10^{-5}	0.9	131,860
12	5.2	4.88×10^{-5}	0.9	18	2.83×10^{-5}	0.9	133,860
18	5.8	4.16×10^{-5}	0.9	19	2.69×10^{-5}	0.9	134,070
24	5.8	3.77×10^{-5}	0.9	20	8.61×10^{-6}	0.9	160,070

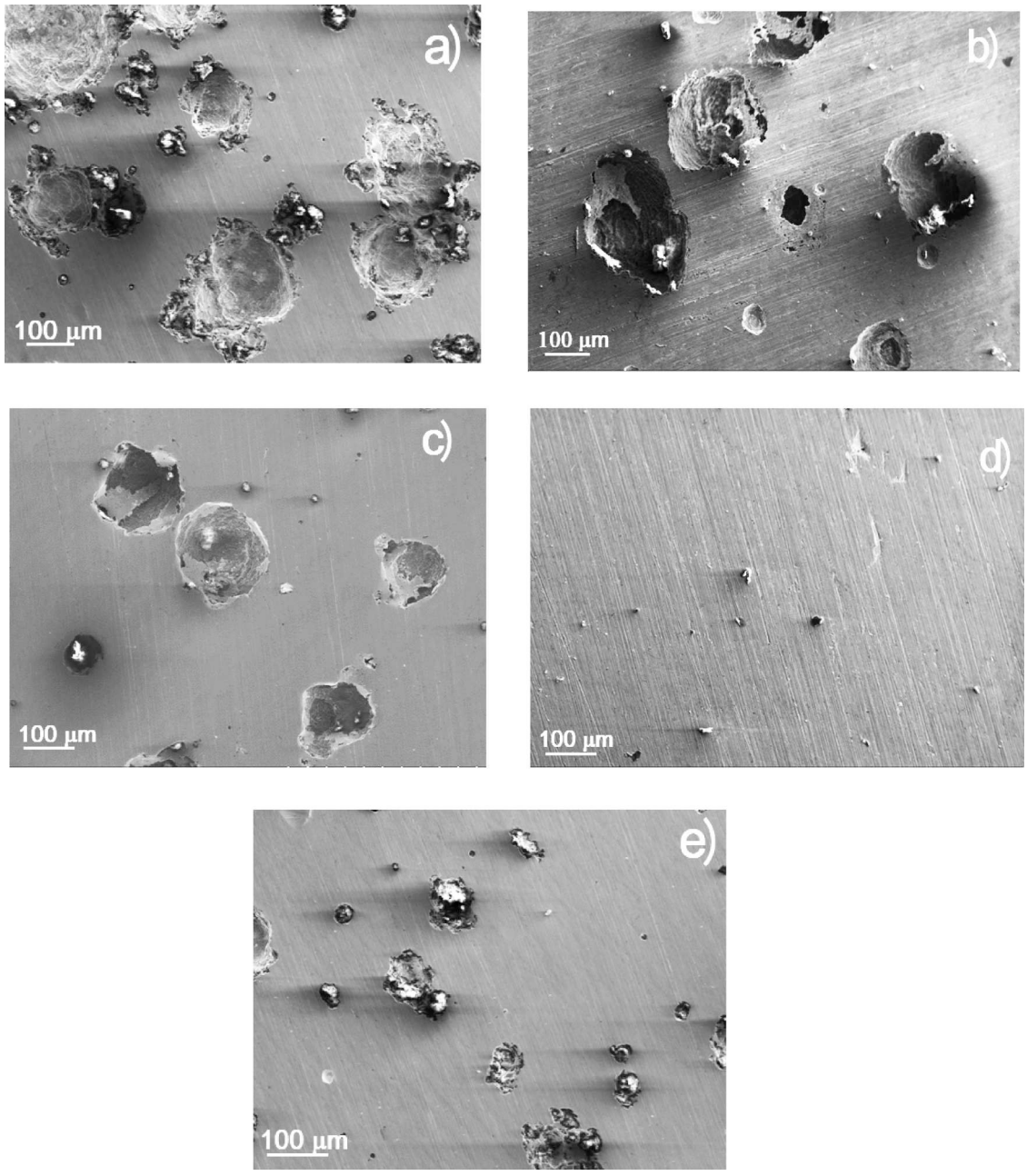

Figure 10. SEM micrographs of LDX 2101 duplex stainless steel corroded in a CO_2-saturated 3.5% NaCl solution containing (a) 0, (b) 200, (c) 400, (d) 600 and (e) 800 ppm of CeO_2 NPs.

number of spherical-shaped pits, with a diameter higher than 100 µm, but as the CeO_2 NPs concentration increased to 200 and 400 ppm, Figure 10b and c, the number of pits and their diameter was gradually decreasing. At a concentration of 600 ppm of CeO_2 NPs, Figure 10d, it is clear the absence of pits, in agreement with the above given results which showed that this was the concentration where the lowest corrosion rate was obtained. When a CeO_2 NPs were added to the solution, Figure 10e, the diameter of the pits was smaller than those found either in the uninhibited solution or with lower CeO_2 NPs concentrations. Since it is not possible to see the nanoparticles to be observed on the corroded steel surface with a normal SEM, we used Raman spectroscopy as shown in Figure 11. This figure shows the Raman spectra of pure CeO_2 NPs and that for duplex stainless steel exposed to the corrosive medium with 600 and 800 ppm of CeO_2 NPs. The spectrum corresponding to pure NPs shows the Raman active mode at 462 cm^{-1} attributed to the symmetric stretching of the Ce-O8 (F2 g) vibrational unit corresponding to a cubic crystalline structure (57). In the

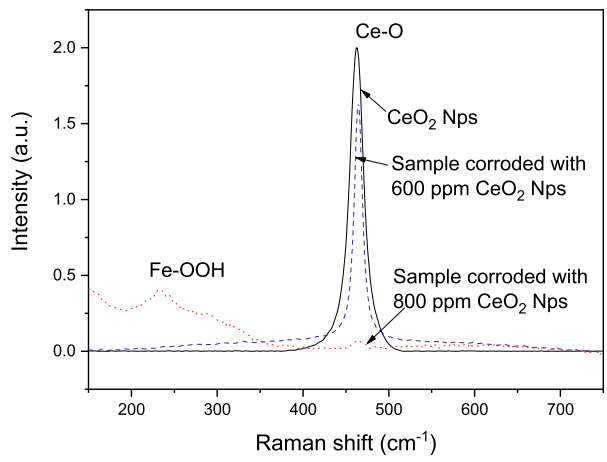

Figure 11. Raman spectrum of pure CeO_2 NPs and LDX 2101 duplex stainless steel corroded in a CO_2-saturated 3.5% NaCl solution containing 600 and 800 ppm of CeO_2 NPs.

Raman spectrum corresponding to steel corroded in presence of 600 ppm CeO_2 NPs, this signal shifts to 465 cm^{-1} due to the chemisorption of the NPs on the steel that reduces the deformation due to the occupation of oxygen vacancies in the Ce^{3+}/Ce^{4+} ratio (59), which corroborates the adsorption of CeO_2 NPs on the surface of duplex stainless steel. This fact indicates that the oxidation state of Ce was not affected ant therefore, other oxides such as Ce_2O_3, CeO, Ce_3O_4 and CeO_3 could not be formed. However, the spectrum that corresponds to the steel corroded in the presence of 800 ppm of CeO_2 nanoparticles shows a small band at 465 cm^{-1} of the symmetrical stretching of CeO_2, which indicates a negligible adsorption of the NPs. However around 235 cm^{-1}, a band corresponding to the vibration of Lepidocrocite γ-FeOOH is observed, probably as corrosion products.

4. Conclusions

A study of the use of CeO_2 NPs as CO_2-corrosion inhibitor for LDX 2101 duplex stainless steel has been carried out. The addition of nanoparticles in to the CO_2-containing solution shifted the OCP value in to the noble direction due to its adsorption and formation of a protective film. Both the corrosion and passivation current density values decreased by two orders of magnitude whereas the pitting potential value became more positive with the addition of the CeO_2 NPs. Inhibition efficiency increased with the CeO_2 NPs concentration reaching its highest value with the addition of 600 ppm, decreasing with a further increase up to 800 ppm. This was due to the chemical adsorption of the NPs according to a Langmuir type of adsorption isotherm. CeO_2 NPs behave as a mixed type of inhibitor affecting both anodic and cathodic electrochemical reactions. The corrosion mechanism was under charge transfer control and was not affected by the addition of the NPs, which decreased the double-layer capacitance and increased the corrosion products film resistance. Steel was highly susceptible to pitting type of corrosion, but the density and size of the pits decreased with the addition of the CeO_2 NPs.

Acknowledgments

The authors of this work, especially Mr. A. Brito-Franco, would like to acknowledge to Conahcyt, Mexico, for the financial support given.

Disclosure statement

No potential conflict of interest was reported by the author(s).

Data availability statement

The raw/processed data required to reproduce these findings are available upon request.

References

[1] El-Lateef, H.M.A. Corrosion Inhibition Characteristics of a Novel Salycilidene Isatin Hydrazine Sodium Sulfonate on Carbon Steel in HCl and a Synergistic Nickel Ions Additive: A Combined Experimental and Theoretical Perspective. *Appl. Surf. Sci.* **2020**, *501*, 144237.

[2] Sousa, V.F.C.; Silva, F.J.G.; Alexandre, R. Experimental Study on the Wear Evolution of Different PVD Coated Tools Under Milling Operations of LDX2101 Duplex Stainless Steel. *Adv. Manuf.* **2023,** *11*, 158–179.

[3] Liu, Z.; Gao, X.; Du, L.; Li, J.; Li, P.; Yu, C.; Misra, R.D.K.; Wang, Y. Comparison of Corrosion Behaviour of low-Alloy Pipeline Steel Exposed to H_2S/CO_2-Saturated Brine and Vapour-Saturated H_2S/CO_2 Environments. *Electrochim. Acta.* **2017,** *232*, 528–541.

[4] Dauthal, P.; Mukhopadhyay, M. Noble Metal Nanoparticles: Plant-Mediated Synthesis, Mechanistic Aspects of Synthesis, and Applications. *Ind. Eng. Chem. Res.* **2016,** *55*, 9557–9577.

[5] Zanotto, F.; Grassi, V.; Balbo, A.; Monticelli, C.; Melandri, C.; Zucchi, F. Effect of Brief Thermal Aging on Stress Corrosion Cracking Susceptibility of LDSS 2101 in the Presence of Chloride and Thiosulphate Ions. *Corros. Sci.* **2018,** *130*, 22–30.

[6] Deng, B.; Jiang, Y.; Xu, J.; Sun, T.; Gao, J.; Zhang, L.; Zhang, W.; Li, J. Application of the Modified Electrochemical Potentiodynamic Reactivation Method to Detect Susceptibility to Intergranular Corrosion of a Newly Developed Lean Duplex Stainless Steel LDX2101. *Corros. Sci.* **2010,** *52*, 969–977.

[7] Rosalbino, F.; Scavino, G.; Ubertalli, G. Electrochemical Corrosion Behavior of LDX 2101 Duplex Stainless Steel

in Fluoride-Containing Environment. *Mater. Corros.* **2020,** *71*, 2021–2028.

[8] Shetty, P. Schiff Bases: An Overview of Their Corrosion Inhibition Activity in Acid Media Against Mild Steel. *Chem. Eng. Comm.* **2020,** *207*, 985–1029.

[9] Benghalia, M.A.; Fares, C.; Khadraoui, A.; Hadj Meliani, M.; Obot, I.B.; Sorrour, A.; Dmytrakh, M.; Azari, Z. Performance Evaluation of a Natural and Synthetic Compound as Corrosion Inhibitors of API 5 l X52 Steel in Hydrochloric Acid Media. *Mor. J. Chem.* **2018,** *6*, 51–61.

[10] Chauhan, D.S.; Quraishi, M.A.; Mazumder, M.A.J.; Ali, S.A.; Aljeaban, N.A.; Alharbi, B.G. Design and Synthesis of a Novel Corrosion Inhibitor Embedded with Quaternary Ammonium, Amide and Amine Motifs for Protection of Carbon Steel in 1 M HCl. *J. Mol. Liq.* **2020,** *317*, 113917.

[11] Gao, M.; Zhang, J.; Liu, Q.; Li, J.; Chen, R.Z.G. Effect of the Alkyl Chain of Quaternary Ammonium Cationic Surfactants on Corrosion Inhibition in Hydrochloric Acid Solution. *C. R. Chimie* **2019,** *22*, 355–362.

[12] Olivares-Xometl, O.; Lijanova, I.V.; Likhanova, N.V.; Arellanes-Lozada, P.; Hernández-Cocoletzi, H.; Arriola-Morales, J. Theoretical and Experimental Study of the Anion Carboxylate in Quaternary-Ammonium-Derived Ionic Liquids for Inhibiting the Corrosion of API X60 Steel in 1 M H_2SO_4. *J. Mol. Liq.* **2020,** *318*, 114075.

[13] Bahlakeh, G.; Ramezanzadeh, M.; Ramezanzadeh, B. Experimental and Theoretical Studies of the Synergistic Inhibition Effects Between the Plant Leaves Extract (PLE) and Zinc Salt (ZS) in Corrosion Control of Carbon Steel in Chloride Solution. *J. Mol. Liq.* **2017,** *248*, 854–870.

[14] Rajendran, S.; Shanmugapriya, S.; Rajalakshmi, T.; Raj, A.J.A. Corrosion Inhibition by an Aqueous Extract of Rhizome Powder. *Corrosion* **2005,** *61*, 685–692.

[15] Eddy, N.O.; Odoemelam, S.A.; Odiongenyi, A.O. Joint Effect of Halides and Ethanol Extract of Lasianthera Africana on Inhibition of Corrosion of Mild Steel in H_2SO_4. *J. Appl. Electrochem.* **2009,** *39*, 849–857.

[16] Rahim, A.A. Mangrove Tannins and Their Flavonoid Monomers as Alternative Steel Corrosion Inhibitors in Acidic Medium. *Corros. Sci.* **2007,** *49*, 402–417.

[17] Bouyanzer, A.; Hammouti, B.; Majidi, L. Pennyroyal oil from Mentha Pulegium as Corrosion Inhibitor for Steel in 1M HCl. *Mater. Lett.* **2006,** *60*, 2840–2843.

[18] Oguzie, E.E.; Njoku, D.I.; A, M. Chidebere Characterization and Experimental and Computational Assessment of Kola Nitida Extract for Corrosion Inhibiting Efficacy. *Ind. Eng. Chem. Res.* **2014,** *53*, 5886–5894.

[19] Oguzie, E.E.; Adindu, C.B.; Enenebeaku, C.K. Natural Products for Materials Protection: Mechanism of Corrosion Inhibition of Mild Steel by Acid Extracts of Piper Guineense. *J. Phys. Chem. C* **2012**, *116*, 13603–13615.

[20] Rybolt, T.R.; Hansel, R.A. Determining Molecule–Carbon Surface Adsorption Energies Using Molecular Mechanics and Graphene Nanostructures. *J. Colloid. Interf. Sci.* **2006,** *300*, 805–808.

[21] Abdrabo, S.W.; Elgendy, B.; Soliman, K.A.; El-Lateef, H.M.A.; Tantawy, A.H. Synthesis, Assessment and Corrosion Protection Investigations of Some Novel Peptidomimetic Cationic Surfactants: Empirical and Theoretical Insights. *J. Molec. Liq.* **2020,** *315*, 113672.

[22] Umoren, S.A.; Madhankumar, A. Effect of Addition of CeO_2 Nanoparticles to Pectin as Inhibitor of X60 Steel Corrosion in HCl Medium. *J. Molec. Liq.* **2016,** *224*, 72–82.

[23] Bahlakeh, G.; Ramezanzadeh, B.; Ramezanzadeh, M. Cerium Oxide Nanoparticles Influences on the Binding and Corrosion Protection Characteristics of a Melamine-Cured Polyester Resin on Mild Steel: An Experimental, Density Functional Theory and Molecular Dynamics Simulation Study. *Corros. Sci.* **2017,** *118*, 69–83.

[24] Motte, C.; Poelman, M.; Roobroeck, A.; Fedel, M.; Deflorian, F.; Olivier, M.-G. Improvement of Corrosion Protection Offered to Galvanized Steel by Incorporation of Lanthanide Modified Nanoclays in Silane Layer. *Prog. Org. Coat.* **2012,** *74*, 326–333.

[25] Rodič, P.; Milošev, I. Corrosion Inhibition of Pure Aluminium and Alloys AA2024-T3 and AA7075-T6 by Cerium(III) and Cerium(IV) Salts. *J. Electrochem. Soc.* **2016,** *163*, C85–C92.

[26] Piro, N.A.; Robinson, J.R.; Walsh, P.J.; Schelter, E.J. The Electrochemical Behavior of Cerium(III/IV) Complexes: Thermodynamics, Kinetics and Applications in Synthesis. *Coord. Chem. Rev.* **2014,** *260*, 21–36.

[27] Harvey, T.G. Cerium-based Conversion Coatings on Aluminium Alloys: A Process Review. *Int. J. Corros. Process. Corros. Control* **2013,** *48*, 248–269.

[28] Simion, C.E.; Florea, O.G.; Florea, M.; Ne atu, F.; Ne atu, S.; Trandafir, M.M.; Stanoiu, A. CeO_2:Mn_3O_4 Catalytic Micro-Converters Tuned for CH4 Detection Based on Catalytic Combustion Under Real Operating Conditions. *Materials. (Basel)* **2020,** *13*, 2196–2205.

[29] Wang, P.; Cai, C.; Tan, J.; Pan, M. Effect of the CeO_2 Nanoparticles in Microporous Layers on the Durability of Proton Exchange Membrane Fuel Cells. *Int. J. Hydrogen Energ.* **2021,** *46*, 34867–34873.

[30] Hul, G.; Gentile, S.R.; Zimmermann, S.; Stoll, S. Towards a Better Understanding of CeO2 Manufactured Nanoparticles Adsorption Onto Sand Grains Used in Drinking Water Treatment Plants. *Colloid. Surf. A Physicochem. Eng. Aspects* **2022,** *646*, 129000.

[31] Chavez-Baldovino, E.; Malca-Reyes, C.A.; Masso, R.; Feng, P.; Camacho, A.; Sarmiento, J.; Borrero Negron, J.I.; Pagan-Torres, Y.J.; Diaz-Vazquez, L.M. Optimizing Sustainable Energy Generation in Ethanol Fuel Cells: An Exploration of Carrageenan with TiO2 Nanoparticles and Ni/CeO_2 Composites. *ACS Omega* **2023,** *8*, 20642–20653.

[32] Vorokhta, M.; Matolínová, I.; Dubau, M.; Haviar, S.; Khalakhan, I.; Ševčíková, K.; Mori, T.; Yoshikawa, H.; Matolín, V. HAXPES Study of CeOx Thin Film–Silicon Oxide Interface. *Appl. Surf. Sci.* **2014,** *303*, 46–53.

[33] Liang, J.; Hu, Y.; Fan, Y.; Chen, H. Formation of Superhydrophobic Cerium Oxide Surfaces on Aluminum Substrate and its Corrosion Resistance Properties. *Surf. Interf. Anal.* **2013,** *45*, 1211–1216.

[34] Hao, L.; Jiang, Z.; Fang, Y.; Zhou, Y.; Fu, B.; Lin, L. Understanding the Role of Oxygen Vacancy on Corrosion Resistance of Coating Containing Cerium Oxide Nanoparticles Doped with Cobalt as Highly Effective Corrosion Inhibitors. *Appl. Surf. Sci.* **2023,** *626*, 157300.

[35] Cai, G.; Hu, P.; Cao, X.; Chen, J.; Zhang, X.; Dong, Z. pH-triggered Self-Inhibition Epoxy Coating Based on Cerium-

Polyphenolic Network Wrapped Carbon Nanotube. *Prog. Org. Coat.* **2023**, *175*, 107355.
[36] Dong, Y.; Zhang, Y.; Cui, X.J.; Li, M.; Xie, C.; Pan, Z. Surface-modified Cerium Oxide as a Corrosion Inhibitor to Enhance the Performance of Epoxy Coatings. *Anti-Corros. Method M* **2023**, *70*, 149–156.
[37] Joseph, A.; Akshay, K.S.; Sajith, V. Synergistic Effect of Ceria-Zirconia Nanoparticles and hBN Nanosheets Incorporation on the Corrosion Resistance of MoS_2 Solid Lubricant Coatings. *Surf. Coat. Technol.* **2023,** *473*, 130025.
[38] He, J.; Ma, L.; Yang, Y.; Jia, W.; Zhou, Q.; Yang, S.; Wang, J. Construction of Fluorinated Graphene/Cerium Oxide Composite Coatings Using Ethylenediamine as the Covalent Interface Adhesive: Lubrication and Anticorrosion Performances. *Tribol. Int.* **2023,** *187*, 108753.
[39] Nawaz, M.; Shakoor, R.A.; Kahraman, R.; Montemor, M.F. Cerium Oxide Loaded with Gum Arabic as Environmentally Friendly Anti-Corrosion Additive for Protection of Coated Steel. *Mater. Des.* **2021,** *198*, 109361.
[40] Fedel, M.; Ahniyaz, A.; Ecco, L.G.; Deflorian, F. Electrochemical Investigation of the Inhibition Effect of CeO_2 Nanoparticles on the Corrosion of Mild Steel. *Electrochim. Acta* **2014,** *131*, 71–78.
[41] Sharmila, R.; Selvakumar, N.; Jeyasubramanian, K. Evaluation of Corrosion Inhibition in Mild Steel Using Cerium Oxide Nanoparticles. *Mater. Lett.* **2013,** *91*, 78–80.
[42] Bourenane, N.; Hamlaoui, Y.; Pedraza, F. Electrochemical Investigation of Ceria Nanoparticles as a Corrosion Inhibitor for Steel in Alkaline Medium. *Mater. Corros.* **2023,** *74*, 1356–1370.
[43] Petek, A.; Kovačič, S. The Influence of Ce3 + Ions on the Corrosion Rate of Tainless Steel in Acidic Solutions of Different pH-Values. *Green Chem. Let. Rev.* **2014,** *7*, 337–341.
[44] Phuong, N.V.; Fazal, B.R.; Moon, S. Cerium- and Phosphate-Based Sealing Treatments of PEO Coated AZ31 Mg Alloy. *Surf. Coat. Technol.* **2017,** *309*, 86–95.
[45] Castano, C.E.; O'Keefe, M.J.; Fahrenholtz, W.G. Cerium-based Oxide Coatings. *Curr. Opin. Solid St. M* **2015,** *19*, 69–76.
[46] Guergova, D.; Stoyanova, E.; Stoychev, D.; Avramova, I.; Stefanov, P. Self-healing Effect of Ceria Electrodeposited Thin Films on Stainless Steel in Aggressive 0.5 mol/L NaCl Aqueous Solution. *J. Rare Earth* **2015,** *33*, 1212–1227.
[47] Harb, S.V.; Trentin, A.; Carneiro de Souza, T.A.; Magnani, M.; Pulcinelli, S.H.; Santilli, C.V.; Hammer, P. Effective Corrosion Protection by eco-Friendly Self-Healing PMMA-Cerium Oxide Coatings. *Chem. Eng. J.* **2020,** *383*, 123219.
[48] Lei, Y.; Qiu, Z.; Tan, N.; Du, H.; Li, D.; Liu, J.; Liu, T.; Zhang, W.; Chang, X. Polyaniline/CeO_2 Nanocomposites as Corrosion Inhibitors for Improving the Corrosive Performance of Epoxy Coating on Carbon Steel in 3.5% NaCl Solution. *Prog. Org. Coat.* **2020,** *139*, 105430.
[49] Wang, G.; Mu, Q.; Chen, T.; Wang, Y. Synthesis, Characterization and Photoluminescence of CeO_2 Nanoparticles by a Facile Method at Room Temperature. *J Alloy Compd.* **2010,** *493*, 202–207.
[50] Chen, Y.; Liu, T.; Chen, C.; Guo, W.; Sun, R.; Lv, S.; Saito, M.; Tsukimoto, S.; Wang, Z. Synthesis and Characterization of CeO_2 Nano-Rods. *Ceram. Int.* **2013,** *39*, 6607–6610.
[51] Zhang, W.; Wang, H.; Lv, C.; Chen, X.; Zhao, Z.; Zhu, Y.Y. Effects of CeO_2 Geometry on Corrosion Resistance of Epoxy Coatings. *Surf. Eng.* **2020**, *36*, 175–183.
[52] Arunachalam, T.; Karpagasundaram, M.; Rajarathinam, N. Ultrasound Assisted Green Synthesis of Cerium Oxide Nanoparticles Using Prosopis Juliflora Leaf Extract and Their Structural, Optical and Antibacterial Properties. *Mater. Sci. Poland* **2017,** *35*, 791–798.
[53] Chelliah, M.; Rayappan, J.B.B.; Krishnan, U.M. Synthesis and Characterization of Cerium Oxide Nanoparticles by Hydroxide Mediated Approach. *J. Appl. Sci.* **2012,** *12*, 1734–1737.
[54] Han, Z.; He, C.; Lian, J.; Zhao, Y.; Chen, X. Effects of Temperature on Corrosion Behaviour of 2205 Duplex Stainless Steel in Carbon Dioxide-Containing Environments. *Int. J. Electrochem. Sci.* **2020,** *15*, 3627–3645.
[55] Zhang, Y.; Zhang, S.; Tan, B.; Guo, L.; Li, H. Solvothermal Synthesis of Functionalized Carbon Dots from Amino Acid as an Eco-Friendly Corrosion Inhibitor for Copper in Sulfuric Acid Solution. *J. Coll. Interf. Sci.* **2021,** *604*, 1–14.
[56] Singh, A.; Lin, Y.; Ebenso, E.E.; Liu, W.; Pan, J.; Huang, B. Gingko Biloba Fruit Extract as an eco-Friendly Corrosion Inhibitor for J55 Steel in CO_2 Saturated 3.5% NaCl Solution. *J. Ind. Eng. Chem.* **2015,** *2*, 219–228.
[57] Saha, S.K.; Murmu, M.; Murmu, N.C.; Banerjee, P. Evaluating Electronic Structure of Quinazolinone and Pyrimidinone Molecules for its Corrosion Inhibition Effectiveness on Target Specific Mild Steel in the Acidic Medium: A Combined DFT and MD Simulation Study. *J. Mol. Liq.* **2016,** *224*, 629–638.
[58] Gouadec, G.; Colomban, P. Raman Spectroscopy of Nanostructures and Nanosized Materials. *J. Raman Spectrosc.* **2007,** *38*, 0377–0486.
[59] Choudhury, B.; Choudhury, A. Ce^{3+} and Oxygen Vacancy Mediated Tuning of Structural and Optical Properties of CeO_2 Nanoparticles. *Mater. Chem. Phys.* **2012,** *131*, 666–671.